

Tuning Interlayer Coupling in Large-Area Heterostructures with CVD-Grown MoS₂ and WS₂ Monolayers

Sefaattin Tongay,^{*,†,‡,¶} Wen Fan,^{†,‡,¶} Jun Kang,[§] Joonsuk Park,^{||} Unsal Koldemir,^{||} Joonki Suh,[†] Deepa S. Narang,[⊥] Kai Liu,[†] Jie Ji,[‡] Jingbo Li,[§] Robert Sinclair,^{||} and Junqiao Wu^{*,†,§,#}

[†]Department of Materials Science and Engineering, University of California, Berkeley, California 94720, United States

[‡]Department of Thermal Science and Energy Engineering, University of Science and Technology of China, Anhui 230027, China

[§]Institute of Semiconductors, Chinese Academy of Sciences, Beijing 100083, China

^{||}Department of Materials Science and Engineering, Stanford University, Stanford, California 94305, United States

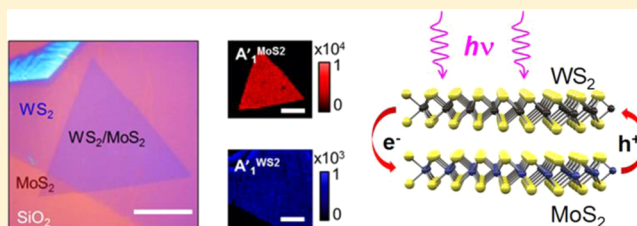
[⊥]Department of Physics, Alliance College of Engineering and Design (ACED), Alliance University, Chandapura, Anekal, Bangalore, 562106, Karnataka, India

[#]Division of Materials Sciences, Lawrence Berkeley National Laboratory, Berkeley, California 94720, United States

S Supporting Information

ABSTRACT: Band offsets between different monolayer transition metal dichalcogenides are expected to efficiently separate charge carriers or rectify charge flow, offering a mechanism for designing atomically thin devices and probing exotic two-dimensional physics. However, developing such large-area heterostructures has been hampered by challenges in synthesis of monolayers and effectively coupling neighboring layers. Here, we demonstrate large-area (>tens of micrometers) heterostructures of CVD-grown WS₂ and MoS₂ monolayers, where the interlayer interaction is externally tuned from noncoupling to strong coupling. Following this trend, the luminescence spectrum of the heterostructures evolves from an additive line profile where each layer contributes independently to a new profile that is dictated by charge transfer and band normalization between the WS₂ and MoS₂ layers. These results and findings open up venues to creating new material systems with rich functionalities and novel physical effects.

KEYWORDS: Monolayer, heterostructure, MoS₂/WS₂, interlayer coupling, 2D materials



Recently, single unit-cell thick semiconducting transition metal dichalcogenides (sTMDs) attracted much interest owing to their unique physical properties. When isolated to monolayers, sTMDs undergo a crossover from indirect bandgap in the bulk to direct bandgap in two-dimensional (2D) monolayers and absorb and emit light rather efficiently.¹ The band structure renormalization as a function of the number of layers originates mostly from relatively strong interlayer coupling, which results in shifts in the conduction and valence band edges at different rates at various symmetry points in the Brillouin zone.^{2–6} Built on the basis of monolayer sTMDs, vertical sTMDs heterostructures formed by stacking up these monolayers offer a rich collection of physics and functionalities. For example, novel, atomically thin charge-separating devices can be envisioned using these heterostructures because of the wide range of bandgaps and band offsets available among these sTMDs.⁷ However, forming sTMD heterostructures with mechanically exfoliated monolayer flakes is impractical, while large-area growth of high-quality sTMD monolayers is still under development.^{8,9}

In this work, we report on formation, tuning, and characterization of large-area, 2D heterostructures using chemical vapor deposition (CVD) - grown MoS₂ and WS₂

monolayers.^{8–11} In these heterostructures, the interlayer coupling can be tuned externally with vacuum annealing, so that the system behaves between the limit of isolated, independent monolayers and the limit of coupled heterobilayers. Our results not only present the first, large-area, bilayer sTMD heterostructures as a material platform to study unusual 2D effects but also offer new venues to control optical properties of sTMDs by externally tuning the interlayer coupling.

WS₂/MoS₂ heterostructures were prepared from CVD grown monolayers using conventional PDMS stamping method (see Methods and Supporting Information Figure S1). In this notation, the former material, WS₂ in this particular case, refers to the top (transferred) monolayer, whereas the latter material (MoS₂) is a monolayer directly grown on the substrate. Figure 1a–e shows typical optical image and Raman/photoluminescence (PL) mapping of a WS₂/MoS₂ heterostructure prepared on SiO₂ (300 nm)/Si substrates. Because the vibrational

Received: February 9, 2014

Revised: May 14, 2014

Published: May 20, 2014

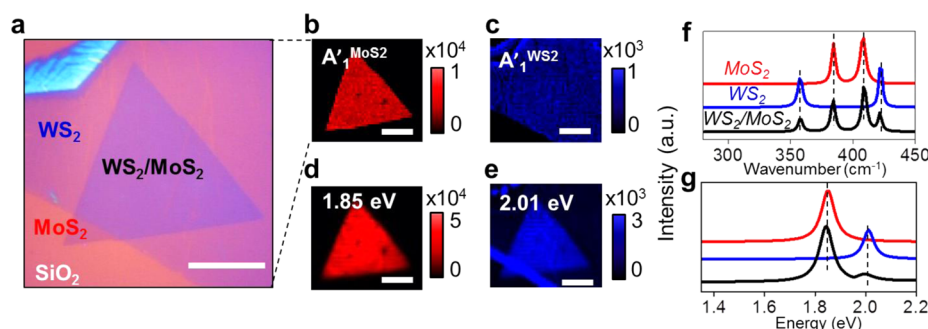


Figure 1. WS₂/MoS₂ heterostructures. (a) Optical image taken from a monolayer WS₂/MoS₂ heterostructure prepared by PDMS stamping CVD-grown WS₂ onto MoS₂ monolayer. (b,c) Raman mapping at the A₁' mode, 408 cm⁻¹ (MoS₂) and 421 cm⁻¹ (WS₂), and (d,e) PL mapping at 1.85 (MoS₂) and 2.01 eV (WS₂). (f) Raman and (g) PL spectra of MoS₂ and WS₂ monolayers and an as-transferred WS₂/MoS₂ heterostructure. The laser excitation used to obtain the three PL spectra has an intensity ratio of 1:5:2. Scale bar is 10 μm in all figures.

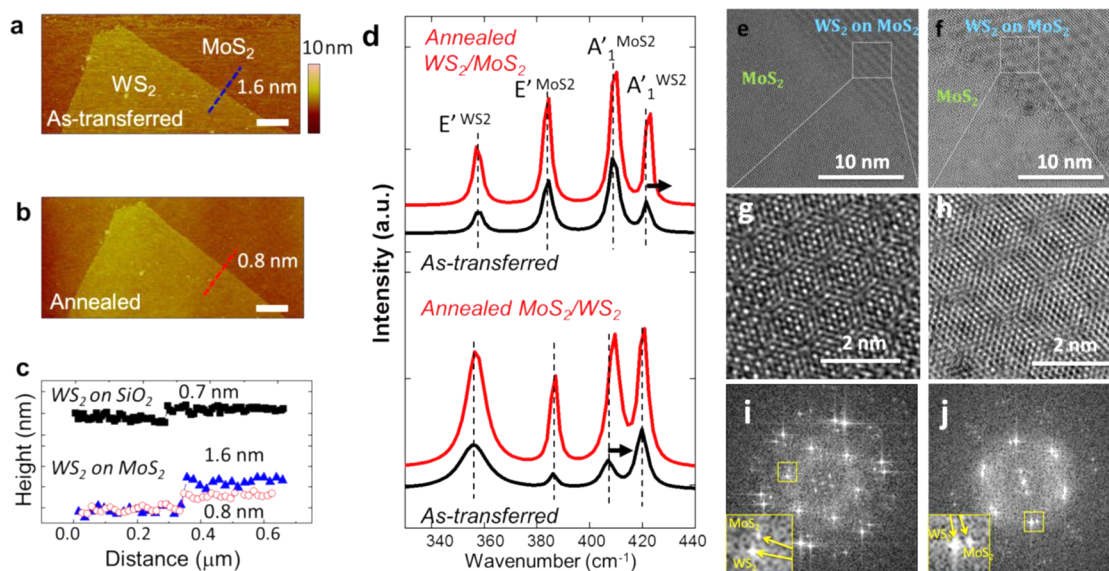


Figure 2. Changes in the interlayer coupling of WS₂/MoS₂ with post-transfer thermal anneal. Tapping mode AFM-measured surface morphology of the heterostructure (a) before and (b) after the thermal annealing. Scale bar, 2 μm. (c) Cross-sectional height profiles of a monolayer WS₂ on SiO₂ surface (black) and on MoS₂ before (blue) and after (red) the thermal anneal. (d) Raman spectrum taken on WS₂/MoS₂ (top panel) and the inverse structure, MoS₂/WS₂ (bottom panel), before and after annealing at 70 °C for 12 h. The arrows highlight the shift of the A₁' Raman peaks. (e,f) HRTEM images of MoS₂/WS₂ heterostructure before and after annealing. (g,h) Zoomed-in images of the MoS₂/WS₂ heterostructure corresponding to the dashed frame in panels e and f, respectively. (i,j) FFT images of the MoS₂/WS₂ heterostructure before and after annealing.

frequencies of MoS₂ and WS₂ are vastly different,^{12,13} Raman mapping clearly shows distinct signal from each of the two layers; in contrast, the ground-state (1s) excitonic light emissions from MoS₂ and WS₂ are relatively close to each other in energy, and mapping at the WS₂ PL peak position (2.01 eV)^{14–17} is shadowed by contributions from the PL shoulder of more luminescent (>2–4 times) MoS₂, as well as the strong edge luminescence in WS₂.¹⁴ The Raman and PL spectra taken on the as-transferred heterostructure can be described as “additive” (Figure 1f,g), that is, each layer contributes independently to the overall signal irrespective of the other layer. This is in stark contrast to exfoliated bilayer sTMDs where the band structure is significantly renormalized to indirect bandgap from direct bandgap in monolayers owing to strong interlayer coupling, which can be described as a relaxation in quantum confinement along the thickness direction.¹ The Raman spectrum of the heterostructure displays in-plane (E') and out-of-plane (A₁') modes of MoS₂ and WS₂ at the same frequencies as in their monolayers;^{18,19} the PL spectrum features two separate emission bands at 1.85 eV from

MoS₂ (P_{MoS₂}) and 2.01 eV from WS₂ (P_{WS₂}) (Figure 1f,g). The lack of band renormalization in as-transferred heterostructures implies that the stacked monolayers behave as if they are isolated from each other and exert negligible amount of influence onto each other. This is observed also in the as-transferred inverse heterostructures, MoS₂/WS₂ (Supporting Information Figure S2).

Indeed, atomic force microscopy (AFM) line scans confirm that these as-transferred heterostructures have an interlayer separation significantly higher than their expected equilibrium value. For example, tapping mode line scans typically yield thickness (step height) around 0.8 nm for monolayers and multiples of 0.8 nm for additional layers.^{8,20–22} On the contrary, the stamped WS₂ monolayer has a step height of ~1.6 nm (Figure 2a) measured from the MoS₂ bottom layer. The large step height can be attributed to unintentional residues trapped between the WS₂ and MoS₂ monolayers during the transfer process. We found that the step height can be reduced from 1.6 nm toward the expected 0.8 nm by mild

vacuum annealing (<0.133 Pa, 120 °C, 6 h) as shown in Figure 2a–c. This is consistent with the possibility that such annealing is able to drive out trapped residual molecules, such as water.²³

From tight-binding theory or quantum tunneling model, the interlayer interaction is expected to be exponentially sensitive to the interlayer distance. As a result, the vibrational modes may stiffen due to increased restoring forces acting onto the layers. However, comparison between the as-transferred and annealed WS₂/MoS₂ heterostructures reveals that only the out-of-plane (A'_1) mode of the top layer (transferred WS₂) stiffens (by a small amount on the order of 4–5 cm⁻¹), while all the other peaks (A'_1 MoS₂, E' MoS₂, and E' WS₂) remain at the same position (Figure 2d top panel). The bottom monolayer MoS₂ is CVD-grown on the substrate, therefore, its vibration is mostly dominated by strong interaction with the substrate, and its A'_1 MoS₂ peak is thus insensitive to the much weaker interlayer coupling with the top WS₂ layer. In-plane modes (E' MoS₂ and E' WS₂) are typically less susceptible to changes in the interlayer coupling¹² and indeed do not display any notable shift after the annealing. The stiffening of the out-of-plane mode of the top WS₂ layer is thus an indication of enhanced interlayer coupling by the annealing. To further test this, we also prepared the inverse heterostructure, MoS₂/WS₂, where the top layer becomes MoS₂ that is transferred onto the bottom, as-grown WS₂ monolayer. In agreement with the expectation, annealing in vacuum again leads to stiffening of the out-of-plane mode of the top layer (A'_1 MoS₂ peak in this case) (Figure 2d).

Our high-resolution transmission electron microscopy (HRTEM) images (Figure 2e–h) show that the annealing step does not induce any structural defects such as phase change on the heterostructures; based on the fast Fourier transform (FFT) images of the heterostructures (Figure 2i,j), there is no evident chemical reaction between the MoS₂ and WS₂ monolayers. In addition, the split spots (inset in Figure 2g,h) confirm the presence of MoS₂ and WS₂ layers. This implies that the observed changes in the optical properties of the heterostructures are attributed to effects arising from changes in interlayer distance by the annealing.

Similar to the observed stiffening in the vibrational spectra, the enhanced interlayer coupling also affects the excitonic light emission of the heterostructures. When the layers are not interacting with each other as in the case of as-transferred heterostructures, the PL is a simple “additive” spectrum with the emission peaks of MoS₂ and WS₂ monolayers independently added together (Figure 3a). Here, we note that the P_{MoS_2} is typically 5–10 times stronger than P_{WS_2} , possibly due to differences in their radiative/nonradiative recombination times and higher density of defects in WS₂ associated with its higher growth temperatures. After annealing the WS₂/MoS₂ heterostructures for different duration times, the PL spectrum gradually changes from additive to “renormalized”. After multiple-peak fitting to the measured PL spectra (for fitting details see Supporting Information Figure S3), the overall trend can be summarized as follows (Figure 3b,c).

(1) A new PL peak (P_{hetero}) emerges at 1.94 eV, and its integrated intensity grows for prolonged annealing time.

(2) Upon the annealing, P_{MoS_2} and P_{WS_2} gradually decrease. After 12 h of annealing, both P_{MoS_2} and P_{WS_2} peaks are barely observable as minuscule features appearing at lower and higher-energy shoulders of the P_{hetero} peak.

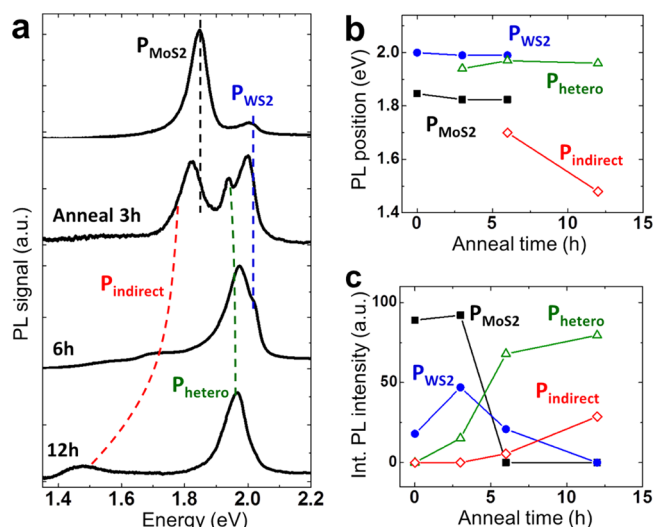


Figure 3. PL of WS₂/MoS₂ heterostructure in response to post-transfer thermal anneal. (a) PL spectrum of an as-transferred WS₂/MoS₂ heterostructure displaying emission from conventional MoS₂ and WS₂ monolayers. After annealing for 3, 6, and 12 h, the PL spectrum is significantly modified: new PL peaks appear at 1.95 eV (P_{hetero}) and at 1.79 eV (P_{indirect}), where the latter eventually shifts down to ~1.50 eV. (b) Evolution of PL peak position and (c) integrated PL intensity of the P_{MoS_2} , P_{WS_2} , P_{hetero} , and P_{indirect} peaks with annealing.

(3) Another weak emission peak (P_{indirect}) appears at 1.75 eV, and the peak position rapidly and eventually red-shifts to ~1.5 eV.

Before we discuss these trends with the density functional theory (DFT) calculations, excitonic interactions, and charge transfer processes, we provide a phenomenological explanation. When monolayers are well separated from each other (as-transferred heterostructures), each layer emits light that is specific to itself, MoS₂ (P_{MoS_2}) or WS₂ (P_{WS_2}). After the annealing, the two monolayers start to electronically couple to each other, and their band structure gradually changes from the isolated limit toward the true heterostructure, bilayer limit. This is manifested in the PL spectrum as a gradual reduction in P_{MoS_2} and P_{WS_2} and appearance of the P_{hetero} and P_{indirect} peaks. Because the P_{indirect} peak position changes rapidly with the degree of coupling (annealing time), we attribute this to phonon-assisted, indirect bandgap transition, which involves the valence band maximum (VBM) at the Γ -point and the conduction band minimum (CBM) at the K-point.² To test this scenario, we also transfer CVD monolayer MoS₂ onto MoS₂, forming MoS₂/MoS₂ homostructures (see Supporting Information Figure S4). These as-transferred MoS₂ homostructures only display emission at P_{MoS_2} . Upon annealing, a new, weak PL peak develops at lower energies and shifts to a position in agreement with the indirect-bandgap, $\Gamma \rightarrow \text{K}$ transition often observed in exfoliated bilayer MoS₂.¹ Indeed, this is consistent with the evolution in the PL spectrum of exfoliated sTMDs from monolayers to multilayers,^{1,2,13,17} where a new, indirect-bandgap emission line emerges for increasing number of layers.

To provide an insight on the observed phenomena, we have carried out DFT calculations on the heterostructures by including the spin–orbit coupling (SOC) interactions. The latter effect is known to be large for monolayer sTMDs and splits the VBM level at the K-symmetry point by 0.15 and 0.4

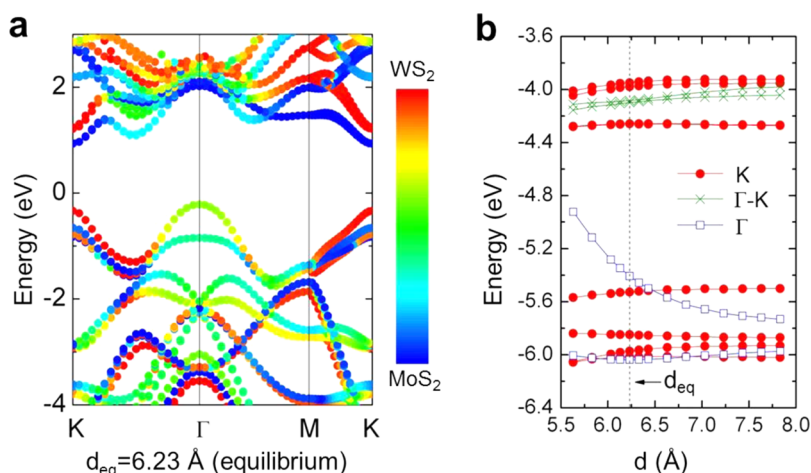


Figure 4. DFT calculations of WS_2/MoS_2 heterostructures and direct to indirect gap transition. (a) Band structure of AB-stacked WS_2/MoS_2 heterostructure at interlayer distance $d = 6.23 \text{ \AA}$ (natural equilibrium state). (b) Energies for the band-edge states as a function of the interlayer distance d . The vertical dotted lines denote distance d at the equilibrium state.

eV for MoS_2 and WS_2 , respectively, as shown in Figure 4a. In Figure 4a, we show the calculated band structure of WS_2/MoS_2 heterostructure at the equilibrium interlayer separation distance ($d = d_{\text{eq}} = 6.23 \text{ \AA}$). On the basis of the orbital character, the valence and conduction bands are displayed using different colors ranging from blue (orbitals contribution from WS_2) to red (MoS_2). These VBM and CBM values depend on the interlayer interaction strength. For example, reduction in the interlayer spacing modifies the VBM and CBM values at high symmetry points as shown in Figure 4b and Supporting Information Figure S5, especially the VBM at Γ -point.

The VBM at Γ (CBM at Γ -K) originates from hybridization between d_{z^2} orbital of Mo or W and p orbital of S ($d_{x^2-y^2}$ of Mo or W and p of S), whereas the VBM (CBM) at the K-point is mostly composed of the Mo- or W- d_{z^2} ($d_{x^2-y^2}$) orbitals. Because of the different orbital character, the VBM and CBM energies at these high symmetry points respond very differently to the interlayer coupling (Supporting Information Figure S5). For example, by varying the interlayer distance, while the VBM and CBM at K-point change only by 50–70 meV (Figure 4b), the VBM at Γ -point involving p-d orbital coupling changes dramatically. Because of such sensitivity of the VBM at the Γ point, we attribute the P_{indirect} emission, which rapidly redshifts with thermal annealing, to phonon-assisted optical transition across the $\Gamma(\text{VBM}) \rightarrow \text{K}(\text{CBM})$ indirect bandgap. On the other hand, the PL peak P_{hetero} at 1.95 eV is approximately 60 meV below P_{WS_2} , and this amount of energy is lower than the accuracy of DFT calculations; therefore, it is difficult to draw a concrete conclusion within the DFT framework regarding the exact origin of the P_{hetero} emission. Here, we note that the strength of the interlayer interaction also depends on interlayer registry such as A–A and A–B (Bernal stacking), and as a result, physical properties of the heterostructures could be affected by the orientation angle between the two layers as observed in graphene and graphitic materials. However, DFT calculations show that once the MX_2 heterostructure reaches the equilibrium distance, different interlayer registry configurations change the VBM at Γ point only by $\sim 50 \text{ meV}$, and do not influence the optical bandgap significantly (Supporting Information Figure S6). Such contrast between graphene and sTMDs heterostructures stems from the fact that the band structure of covalently bonded graphene is exponentially

sensitive to the coupling between p_z orbitals. In contrast, in sTMDs, the VBM and CBM at K-point is dictated by in-plane metal-chalcogen bonding, and the VBM at Γ -point is relatively insensitive to orientation angle at the equilibrium distance as a result of weak interaction between d_{z^2} and p_z orbitals with low charge densities. Consistent with these discussions, 2D heterostructures with randomly different orientation angles do not exhibit detectably different PL spectrum.

To elucidate the P_{hetero} emission, we consider excitonic effects and ultrafast charge relaxation across the heterostructure. On the basis of DFT calculations,⁷ the WS_2/MoS_2 heterostructure forms a type-II band alignment in equilibrium condition, where the VBM and CBM of WS_2 are higher than that of MoS_2 (Figure 5b). For this type of band-alignment, large electric field develops across the $\sim 1 \text{ nm}$ thick junction; this leads to strong exciton splitting by which holes (electrons) are rapidly swept from MoS_2 to WS_2 (from WS_2 to MoS_2). Assuming that the hole mobility (μ_h) is $\sim 0.1 \text{ cm}^2/(\text{V s})$, the time it takes for holes to drift from MoS_2 to WS_2 is given by $\tau_h =$

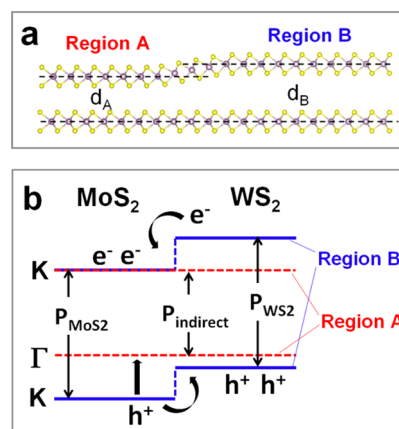


Figure 5. Band alignment and charge transfer at the heterostructures. (a) Schematic of the heterostructures displaying strongly coupled (A) and weakly coupled (B) regions with interlayer spacing of d_A and d_B , respectively. Here $d_{\text{eq}} \leq d_A < d_B$ where the d_{eq} is the interlayer distance at equilibrium. (b) The band alignment at the K-point for the WS_2/MoS_2 heterostructure in Region B, and at the Γ - (VBM) and K- (CBM) points in Region A.

$d^2/[\mu_h \cdot \Delta(\text{VBM})] \sim 0.3$ ps (Figure 5b). This time scale is significantly shorter than typical recombination lifetimes in these materials.²⁴ Therefore, the MoS₂ (WS₂) monolayer in the heterostructure is expected to be immediately depleted of holes (electrons) and accumulated of electrons (holes). It has been established^{25–28} that heavy accumulation with electrons in these monolayer semiconductors would favor the formation of negatively (positively) charged exciton, namely, eeh or X[−] trion (ehh or X⁺ trion); as such, the trion recombination emission intensity would grow at the cost of the neutral exciton (eh) recombination emission intensity. The trion peak is redshifted from the neutral exciton by an amount given by the binding energy of the extra free carrier to the neutral exciton, ranging from 30 to 60 meV at room temperature depending on the Fermi level.²⁵

On the basis of this analysis, we attribute the P_{hetero} peak to X⁺_{WS₂} in the heavily hole-accumulated WS₂ monolayer, which is approximately 60 meV below the original P_{WS₂} peak (X⁰_{WS₂}). However, this model equally considers MoS₂ and WS₂; therefore, it does not explain the different behavior of MoS₂ in the heterostructure, that is, the gradual disappearance of the P_{MoS₂} peak but in absence of a trion peak, X[−]_{MoS₂}, emitted from the electron accumulated MoS₂ monolayer.

On the basis of our earlier discussions, we speculate that the thermal annealing gradually drives out liquid residues trapped between the layers, and possibly causes a spatially inhomogeneous 2D heterostructure composed of strongly (Region A) and weakly (Region B) coupled regions (Figure 5a). In Region A, the interlayer distance is close to the equilibrium value d_{eq} and the VBM at Γ in Region A becomes higher than MoS₂ VBM at K in Region B (Figure 4b). As a result, Region A acts as a hole funnel where the holes in the heterostructure are not only swept to WS₂, but also to the VBM of region A (Figure 5b). This process further drains the remaining holes from the MoS₂ layer in addition to the earlier hole transfer from MoS₂ to WS₂, leading to quenching of both eh and eeh emissions in MoS₂ across the entire 2D heterostructure. In contrast, the CBM of Region A stays at the same level as in Region B for both MoS₂ and WS₂ (Figures 4 and 5b), because the CBM energy level at the K symmetry point is dominated by orbital coupling between in-plane d orbitals of metal and in-plane p orbitals of chalcogen atoms, naturally insensitive to the interlayer coupling. As a result and unlike the case of MoS₂, remaining electrons in WS₂ are not funneled to region A, and ehh (trion) emission from the WS₂ layer remains relatively unaffected by the spatially inhomogeneous interlayer coupling. Therefore, the asymmetric behavior in trion emissions from MoS₂ and WS₂ layers originates fundamentally from the different bonding character in the heterostructure.

In summary, we have demonstrated large-area 2D heterostructures formed using CVD-grown monolayer WS₂ and MoS₂ where the interlayer coupling could be tuned by vacuum thermal annealing. As a function of the coupling strength, the light emission evolves gradually from an additive spectrum, that is, MoS₂ and WS₂ monolayers contribute separately to the light emission of the heterostructure, to coupled spectrum where the light emission is dictated by charged exciton recombination and phonon-assisted, indirect-bandgap transition. Our results highlight the significance of interlayer coupling and charge transfer in tuning the light emission and absorption of sTMDs and offer a general route to prepare large-area sTMD tandem structures

for fundamental study as well as electronic and photovoltaic applications.

Methods. Sample Preparation. The MoS₂ and WS₂ monolayers were grown at by high-pressure CVD technique (see Supporting Information) at 690 °C for 5 min onto SiO₂/Si substrates.⁸ Heterostructures were prepared using PDMS stamping technique as below. PDMS was spin coated on CVD grown monolayer WS₂/SiO₂/Si and cured at 120 °C for >3 h. PDMS/WS₂/SiO₂/Si sample is baked at 70 °C for 2 h to eliminate air bubbles formed at the monolayer WS₂ and PDMS interface and to increase the adhesion between WS₂–PDMS. PDMS/WS₂ sample is separated from the SiO₂/Si substrate by mildly etching SiO₂ in 1 mol/L KOH solution for 0.5–2 h. PDMS/WS₂ sample is transferred to DI water to reduce KOH residue, and then it is transferred onto CVD grown monolayer MoS₂ on SiO₂/Si substrate for 5 min using long-distance microscope (Stamping process). Afterward, PDMS substrate is peeled off slowly from the SiO₂/Si substrate, leaving the monolayer WS₂ on top of MoS₂ (see Supporting Information), as shown in Figure 1a.

Raman/PL Spectroscopy and AFM Measurements. Heterostructures were measured using commercially available Raman/PL spectrometer (Renishaw Inc.) with 488 nm laser source. Raman and PL measurements were taken on a 5 μm^2 laser spot size with 10 μW power. Samples were characterized using commercially available AFM (Veeco Inc.) in contact mode.

Transmission Electron Microscopy (TEM) Measurements. HRTEM and TEM-electron energy loss spectroscopy (EELS) measurements were performed on the WS₂/MoS₂ heterostructures using FEI Titan 80–300 environmental TEM operated at 80 kV. EELS measurements show that W M3 edge is present in the studied region implying that the WS₂/MoS₂ heterostructure exists (Supporting Information, Figure S7).

DFT Calculations. DFT calculations were performed using Vienna ab initio simulation package.²⁹ The six outer-most electrons for transition-metal and chalcogen atoms were treated as valence electrons. The core–valence interaction was described by the frozen-core project or augmented wave method.³⁰ The generalized gradient approximation of Perdew–Burke–Ernzerh³¹ was adopted for exchange–correlation functional. Energy cutoff for plane-wave expansion was set to 400 eV. Brillouin zone sampling was performed with Monkhorst–Pack special K-point meshes.

■ ASSOCIATED CONTENT

§ Supporting Information

Experimental, Methods, additional DFT calculation and Photo images, and additional measurements. This material is available free of charge via the Internet at <http://pubs.acs.org>.

■ AUTHOR INFORMATION

Corresponding Authors

*E-mail: (S.T.)tongay@berkeley.edu.

*E-mail: (J.W.)wuj@berkeley.edu.

Author Contributions

The manuscript was written through contributions of all authors. All authors have given approval to the final version of the manuscript.

Author Contributions

[†]S.T. and W.F. contributed equally.

Notes

The authors declare no competing financial interest.

ACKNOWLEDGMENTS

This work was supported by the National Science Foundation under Grant DMR-1306601. W.F. and J.J. acknowledge support from the National Science Foundation of China (NSFC) under Contract No. 51206158, and the “First-Class General Financial Grant from the China Postdoctoral Science Foundation” under Contract No. 2011MS00112.

REFERENCES

- (1) Mak, K. F.; Lee, C.; Hone, J.; Shan, J.; Heinz, T. F. *Phys. Rev. Lett.* **2010**, *105* (13), 136805.
- (2) Tongay, S.; Zhou, J.; Ataca, C.; Lo, K.; Matthews, T. S.; Li, J.; Grossman, J. C.; Wu, J. *Nano Lett.* **2012**, *12* (11), 5576–5580.
- (3) Tongay, S.; Sahin, H.; Ko, C.; Luce, A.; Fan, W.; Liu, K.; Zhou, J.; Huang, Y.-S.; Ho, C.-H.; Yan, J.; Ogletree, F.; Li, S.; Li, J.; Peeters, F. M.; Wu, J. *Nat. Commun.* **2014**, *5*, 3252.
- (4) Komsa, H. P.; Krashinsky, A. V. *Phys. Rev. B* **2013**, *88* (8), 085318.
- (5) Kang, J.; Li, J.; Li, S.; Xia, J.; Wang, L. *Nano Lett.* **2013**, *13* (8), 5485–5490.
- (6) Wang, Q. H.; Kalantar-Zadeh, K.; Kis, A.; Coleman, J. N.; Strano, M. S. *Nat. Nanotechnol.* **2012**, *7* (11), 699–712.
- (7) Terrones, H.; Lopez-Urias, F.; Terrones, M. *Sci. Rep.* **2013**, *3*, 1549.
- (8) Zhang, X.-Q.; Zhang, W.; Chang, M.-T.; Lin, C.-T.; Chang, K.-D.; Yu, Y.-C.; Wang, J. T.-W.; Chang, C.-S.; Li, L.-J.; Lin, T.-W. *Adv. Mater.* **2012**, *24* (17), 2320–2325.
- (9) Zhan, Y. J.; Liu, Z.; Najmaei, S.; Ajayan, P. M.; Lou, J. *Small* **2012**, *8* (7), 966–971.
- (10) Van Der Zande, A. M.; Huang, P. Y.; Chenet, D. A.; Berkelbach, T. C.; You, Y.; Lee, G.-H.; Heinz, T. F.; Reichman, D. R.; Muller, D. A.; Hone, J. C. *Nat. Mater.* **2013**, *12* (6), 554–561.
- (11) Zhang, Y.; Zhang, Y.; Zhang, Y.; Ji, Q.; Ju, J.; Yuan, H.; Shi, J.; Gao, T.; Ma, D.; Liu, M.; Chen, Y.; Song, X.; Hwang, H. Y.; Cui, Y.; Liu, Z. *ACS Nano* **2013**, *7* (10), 8963–8971.
- (12) Lee, C.; Yan, H.; Brus, L. E.; Heinz, T. F.; Hone, J.; Ryu, S. *ACS Nano* **2010**, *4* (5), 2695–2700.
- (13) Zhao, W.; Ghorannevis, Z.; Chu, L.; Toh, M.; Kloc, C.; Tan, P.-H.; Eda, G. *ACS Nano* **2013**, *7* (1), 791–797.
- (14) Gutierrez, H. R.; Perea-Lopez, N.; Elias, A. L.; Berkdemir, A.; Wang, B.; Lv, R.; Urias-Lopez, F.; Crespi, V. H.; Terrones, H.; Terrones, M. *Nano Lett.* **2013**, *13* (8), 3447–3454.
- (15) Tongay, S.; Suh, J.; Ataca, C.; Fan, W.; Luce, A.; Kang, J. S.; Liu, J.; Ko, C.; Raghunatan, R.; Zhou, J.; Ogletree, F.; Li, J.; Grossman, J. C.; Wu, J. *Sci. Rep.* **2013**, *3*, 2657.
- (16) Plechinger, G.; Mann, J.; Preciado, E.; Barroso, D.; Nguyen, A.; Eroms, J.; Schuller, C.; Bartels, L.; Korn, T. *Semicond. Sci. Technol.* **2014**, *29*, 064008.
- (17) Tonndorf, P.; Schmidt, R.; Bottger, P.; Zhang, X.; Borner, J.; Liebig, A.; Albrecht, M.; Kloc, C.; Gordan, O.; Zahn, D. R. T.; Vasconcellos, S. M.; Bratschkitsch, R. *Opt. Express* **2013**, *21* (4), 4908–4916.
- (18) Luo, X.; Zhao, Y.; Zhang, J.; Toh, M.; Kloc, C.; Xiong, Q.; Quak, S. Y. *Phys. Rev. B* **2013**, *88*, 195313.
- (19) Terrones, H.; Corro, E. D.; Feng, S.; Poumirol, J. M.; Rhodes, D.; et al. *Sci. Rep.* **2014**, *4*, 4214.
- (20) Wu, S.; Ross, J. S.; Liu, G.-B.; Aivazian, G.; Jones, A.; Fei, Z.; Zhu, W.; Xiao, D.; Yao, W.; Cobden, D.; Xu, X. *Nat. Phys.* **2013**, *9* (3), 149–153.
- (21) Li, H.; Yin, Z.; He, Q.; Loi, H.; Huang, X.; Lu, G.; Fam, D. W. H.; Tok, A. L. Y.; Zhang, Q.; Zhang, H. *Small* **2012**, *8* (1), 63–67.
- (22) Huang, X.; Zeng, Z.; Zhang, H. *Chem. Soc. Rev.* **2013**, *42* (5), 1934–1946.
- (23) Diaz, H. C.; Addou, R.; Batzill, M. *Nanoscale* **2014**, *6* (2), 1071–1078.
- (24) Mak, K. F.; He, K.; Shan, J.; Heinz, T. F. *Nat. Nanotechnol.* **2012**, *7* (8), 494–498.
- (25) Mak, K. F.; He, K.; Lee, C.; Lee, G. H.; Hone, J.; Heinz, T. F.; Shan, J. *Nat. Mater.* **2013**, *12* (3), 207–211.
- (26) Ross, J. S.; Wu, S.; Yu, H.; Ghimire, N. J.; Jones, A. M.; Aivazian, G.; Yan, J.; Mandrus, D. G.; Xiao, D.; Yao, W.; Xu, X. *Nat. Commun.* **2013**, *4*, 1474.
- (27) Tongay, S.; Zhou, J.; Ataca, C.; Liu, J.; Kang, J. S.; Matthews, T. S.; You, L.; Li, J.; Grossman, J. C.; Wu, J. *Nano Lett.* **2013**, *13* (6), 2831–2836.
- (28) Newaz, A. K. M.; Prasai, D.; Ziegler, J. I.; Caudel, D.; Robinson, S.; Haglund, R. F.; Bolotin, K. I. *Solid State Commun.* **2013**, *155*, 49–52.
- (29) Kress, G.; Furthmüller, J. *Phys. Rev. B* **1996**, *54* (6), 11169.
- (30) Perdew, J. P.; Burke, K.; Ernzerhof, M. *Phys. Rev. Lett.* **1996**, *77* (18), 3865.
- (31) Grimme, S. J. *Comput. Chem.* **2006**, *27* (15), 1787–1799.